

Adsorbate-geometry determination by measurement and analysis of angle-resolved-photoemission extended-fine-structure data: Application to $c(2 \times 2)\text{S}/\text{Ni}(001)$

J. J. Barton, C. C. Bahr, S. W. Robey, Z. Hussain,* E. Umbach,† and D. A. Shirley
Materials and Molecular Research Division, Lawrence Berkeley Laboratory, University of California,
Berkeley, California 94720,
and Departments of Chemistry and Physics, University of California, Berkeley, California 94720

(Received 18 February 1986)

We describe our procedures for deducing adsorbate geometry from angle-resolved core-level photoemission measurements as they are applied to $c(2 \times 2)\text{S}/\text{Ni}(001)$. Extracting the energy-dependent, oscillating part of the sulfur ($1s$) photoemission partial cross section gives the angle-resolved-photoemission extended fine structure (ARPEFS). Fourier transformation of the ARPEFS yields peaks at distances characteristic of the local site geometry and in most cases closely related to geometrical path-length differences. Multiple-scattering, curved-wave calculations are fitted to Fourier-filtered data for quantitative geometry determination; the Fourier filtering reduces the size of the scattering cluster and the number of free parameters in the fit. Possible sources of error in this first ARPEFS measurement are discussed as a guide for future work. We find a S–Ni bond length of 2.19 Å ($d_1 = 1.31$ Å), a S–Ni second-layer bond length of 3.14 Å corresponding to a 4% expansion of the top Ni layer, and some evidence that those Ni atoms in the second Ni layer lying beneath sulfur atoms are pulled closer to the sulfur, leading to a buckled second layer.

I. INTRODUCTION

Recently, we reported¹ a new approach to determining surface geometries using high-kinetic-energy, long-energy-range photoelectron diffraction measurements. Experimentally we measure a series of angle-resolved core-level photoemission spectra. Thus we begin with the surface sensitivity and chemical specificity of photoemission; the angle resolution adds geometrical selectivity. As we increase the photoelectron kinetic energy, we observe intensity oscillations about an average atomlike cross section. For electron energies from 50–500 eV, the origin of these partial cross-section oscillations—interference between direct and scattered photoelectron waves—directly relates to the total cross-section oscillations, the extended x-ray-absorption fine structure (EXAFS).^{2,3} Like EXAFS, this type of photoelectron diffraction measurement can be expressed as interference oscillations whose frequency is dominated by geometrical path-length differences and these oscillations can be frequency analyzed to display the structure information directly. To suggest these close connections and to distinguish our new approach from other techniques which use photoelectron diffraction, we refer to the modulations in photoemission partial cross section above 50 eV as angle-resolved-photoemission extended fine structure (ARPEFS).

In this paper we discuss the analysis of S($1s$) ARPEFS measured along the [011] and [001] crystallographic directions from a $c(2 \times 2)$ sulfur overlayer on Ni(001) crystal surface. The nominal geometrical structure of this overlayer is well known.^{4–6} Our purpose in this paper is to report, in detail, procedures we have developed to extract the geometry of S on Ni, including the distance between the S and the second-Ni-layer atoms, from angle-resolved photoemission intensity measurements. We hope to

demonstrate that these same procedures provide a basis for determining the structures of more complicated adsorbate systems. Furthermore, we discuss sources of systematic and random error which could lead to incorrect or inaccurate structures.

A simple elastic scattering theory for ARPEFS (Ref. 1) predicts that angle-resolved photoemission intensity I oscillates about the atomic partial cross section I_0 according to

$$I = I_0(1 + \chi),$$

$$\chi(k) = \sum_j A_j(k) \cos[k(r_j - r_j \cos \theta_j) + \phi_j], \quad (1)$$

where $A_j(k)$ contains the elastic-scattering amplitude, inelastic damping, aperture integration, and thermal averaging, r_j is the bond length, θ_j is the scattering angle, ϕ_j is the scattering phase function, and the sum is over all scattering atoms j with significant amplitude. Our task then is to measure I , the photoemission intensity, convert it to $\chi(k)$, and extract the path-length difference ($r_j - r_j \cos \theta_j$). These three steps correspond to the three main sections of this paper. We describe the photoemission measurements in Sec. II, the extraction of the oscillating signal from the raw data in Sec. III, and the frequency analysis and geometry determination in Sec. IV. Throughout our discussion we shall point out potential sources of inaccuracy and imprecision as a guide to those seeking surface crystallographic structures with chemically significant accuracy.

II. ANGLE-RESOLVED PHOTOEMISSION FROM $c(2 \times 2)\text{S}/\text{Ni}(001)$

The various experimental aspects of these ARPEFS studies are discussed separately in the Secs. II A–II E.

A. Sample

The $c(2 \times 2)$ overlayer of S on Ni(001) has become one of the prototype surface structure problems both because of its importance and because of easy preparation. The bonding of sulfur to Ni crystals is of technological importance primarily because sulfur degrades Ni-based catalysts.⁷ The $c(2 \times 2)$ overlayer is easy to prepare either⁸ by segregation of bulk sulfur impurity or by decomposition of H_2S or (S_2^{2-}) on the Ni surface. Thus the geometry of this surface system has been studied by low-energy electron diffraction (LEED),⁴ surface EXAFS,⁶ normal photoelectron diffraction,⁵ and azimuthal photoelectron diffraction.⁹ Our primary concerns in selecting a system for the first ARPEFS measurements were a well-known structure and a wide accessible energy range above a 1s absorption threshold. The $c(2 \times 2)S/Ni(001)$ is ideally suited for these reasons.

The Ni crystal was cut on a diamond saw from a $\frac{1}{4}$ -in.-diameter boule, oriented, and polished to $< \frac{1}{2}^\circ$ from the perfect (001) face. The final polish with 0.05- μm mesh Al_2O_3 powder in ethanol was followed by a 10-sec etch.¹⁰ The Ni crystal was strapped to a resistively heated Ta sample block by 0.005-in. Ta strips spot welded to the sample block; the sample block was suspended on a three-axis manipulator. Argon-ion sputtering was effective in removing surface sulfur contamination, but each annealing cycle segregated sulfur to the surface. Thus repeated cycles of annealing to 800°C and sputtering were used. When the sulfur was depleted, the crystal was exposed to 0.5 L O_2 and annealed to approximately 750°C. [1 langmuir (L) $\equiv 10^{-6}$ Torr sec.] Experience showed that this step removes surface carbon but leaves no oxide behind. Prior to H_2S exposure the final clean crystal was not examined by Auger or LEED to avoid electron beam-induced deposition of carbon.

The Ni crystal was exposed to ~ 2 L H_2S gas from a 5- μm aperture in front of the sample. Mass spectra of the chamber background gas during dosing showed an increase in H_2 gas at the beginning of the gas exposure. Heating the Ni crystal to $\sim 200^\circ C$ produced a sharp $c(2 \times 2)$ overlayer LEED pattern.

B. Electron energy analyzer

The angle-resolving photoemission analyzer used for these measurements has been previously described.¹¹ Its important features for these measurements are the following: (i) complete two-axis motion allowing an unhindered selection of angles, (ii) multichannel energy analysis for rapid measurements with synchrotron light, and (iii) maximum $\pm 3^\circ$ angular resolution. The angle resolution increases for kinetic energies (E_k) greater than the pass energy ($E_p = 160$ eV) to $\sim \pm 2^\circ$ at $E_k = 400$ eV and the transmission of the analyzer¹² falls like (E_p/E_k) . The analyzer was operated for maximum transmission giving an energy resolution of ~ 1 eV.

C. Photon monochromator

These S(1s) photoemission measurements were made possible by the Stanford Synchrotron Radiation

Laboratory's ultrahigh-vacuum soft-x-ray double-crystal monochromator.¹³ The Ge(111) monochromator crystals gave high flux ($\sim 5 \times 10^{10}$ photons/sec) with 1.1×10^3 resolving power for the 2.5–2.9 keV range used for these measurements. No detectable scattered light entered the sample chamber. The light is highly polarized ($> 95\%$) in the horizontal plane.

D. Photoemission measurements

Two separate experimental geometries were used. In the first, which we call [011], the Ni(001) crystal was rotated about the sample normal to place a [011] axis in the plane of polarization with the [011] direction parallel to the polarization vector. The angle-resolved detector was aligned with the [011] axis; the emission and polarization vector directions were thus collinear. In the second experiment, on a different crystal, the polarization vector was pointed 30° from the crystal normal in a [100] direction, and the analyzer was oriented for normal emission.

With a photon energy of 2504 eV, the electron emission spectrum was measured for 40–500 eV. This provides the electron inelastic-scattering profile and the electron energy analyzer transmission function shown in Fig. 1. For photon energies between 2535 and 2894 eV, sulfur (1s) core-level photoemission measurements were made every 3 eV by advancing both the photon energy with the double-crystal monochromator and the electron energy with the energy analyzer, maintaining the relation $h\nu - 2474$ eV = E_k for the S(1s) peak energy. A typical spectrum is shown inset in Fig. 1. Thus a set of 120 photoemission spectra for each of two directions constitutes our data for the structure analysis.

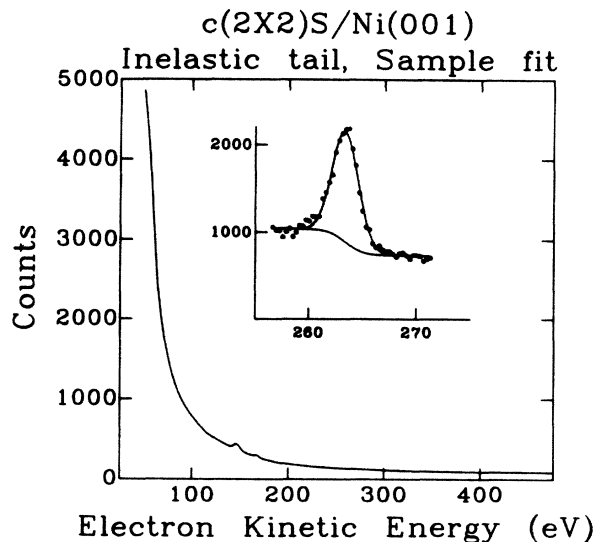


FIG. 1. Inelastic scattered electron background spectrum for $h\nu = 250$ eV and, inset, a simple least-squares fit to a S(1s) photoemission peak. The small features near 174 eV in the background spectrum are S Auger peaks. In the inset, the solid circles are the measured photoemission counts, the upper solid curve gives the fitted function values, while the lower solid curve is the sum of the smoothed background spectrum and the error function step. The photopeak area is the area between the solid curves.

E. Possible sources of error

Errors in the experimental measurements of angle-resolved core-level photoemission limit the ultimate accuracy of our geometry determination. The most serious problem is the accurate angular placement of the polarization and emission direction vectors.

The polar angle of emission with respect to the crystal normal is the most important angle for geometry determination. This angle is determined by the electron analyzer two-axis goniometer and the sample position. The analyzer goniometer was mechanically ruled and aligned;¹¹ it should be reproducible to $<0.2^\circ$, but its accuracy is limited if the sample is not placed at the center of the goniometer rotation. The sample position is determined by maximizing the photoelectron count rate; magnetic fields, incorrect alignment of the electron optics on the goniometer, and misplacement of the photon beam can lead to a sample position away from the chamber center. The sample polar angle is calibrated by laser autocollimation on the polished face of the crystal. The optical surface should be $\pm 1/2^\circ$ from the ideal (001) face. The laser autocollimation is referred to the surface of a vacuum chamber window; the angle between the window and the analyzer goniometer must be inferred from the construction of the window and the vacuum chamber. Once calibrated, the sample position is determined by rotation of a sample manipulator; errors may be introduced if the crystal does not lie on the axis of rotation or if liquid-nitrogen cooling coils or electrical wires apply torque to the sample while it is reoriented. Combined, these errors may well be as large as $\pm 2^\circ$, although some geometries, e.g. normal incidence light, normal emission, or sample normal oriented perpendicular to the autocollimation reference window, can be double checked more easily.

The azimuth of emission and polarization is determined by visual alignment of LEED spots with respect to the vacuum chamber base; although fairly crude, this procedure can be rather precise. The LEED spots report the surface crystallography directly and only a strong magnetic field across the LEED apparatus axis would affect the azimuthal position of these spots; spots separated by ~ 10 cm can be aligned to within ± 1 mm to give a 1° error.

Other errors in the photoemission measurements primarily affect the measured ARPEFS amplitude and not the oscillation frequency. Steps on the crystal surface, impurities, or an improper dose of H_2S atoms will lead to S photoemission not representative of an ordered overlayer; this will typically reduce the measured oscillations as they are expressed as a fraction of the partial cross section for photoemission from any sulfur atom.

The polarization vector position is less important for surface geometry. The synchrotron light is polarized in the horizontal plane. Since the position of our sample is referred to our vacuum chamber, we place the vacuum chamber along the photon beam by centering the beam at the entrance to the chamber and at the electron analyzer on phosphorescent screens. The rotation of the chamber about the beam is then set with a mechanical level. It is difficult to estimate the final error in alignment, but the most sensitive angle—the rotation about the beam—can

be reproduced to $<1^\circ$.

Although this catalog of errors is a rather dreary list, it is roughly the state-of-the-art in angle-resolved-photoemission measurements with synchrotron radiation. In reviewing this list one should recall that the apparatus used for this first ARPEFS measurements was not designed for high-precision structure determination. The more serious problems detailed above can be remedied easily now that their importance is understood. Other methods of surface crystallography must overcome similar difficulties.¹⁴

III. THE EXTENDED FINE STRUCTURE

A. Method

From the raw photoemission measurements we must derive the oscillations in the partial cross section. We have developed a three-step procedure which relies only on photoemission measurements. These steps are the following:

- (i) estimation of the photoemission intensity at each kinetic energy by nonlinear least-squares fits to a simple line-shape function,
- (ii) normalization of these intensities for photon flux and electron analyzer transmission variations using background intensity measurements, and
- (iii) estimation and removal of the atomic partial cross section, I_0 .

In this section we examine each of these steps in detail.

Before proceeding, we pause to discuss the energy scales involved in the analysis. Our raw data consists of a series of photoemission spectra for increasing photon energy $h\nu$. Each spectrum is centered on the sulfur $1s$ core-level photopeak but includes ~ 10 eV of the electron emission spectrum to higher and to lower kinetic energy. The photopeak mean kinetic energy E is related by the $S(1s)$ binding energy E_B to the photon energy $h\nu$:

$$E = h\nu - E_B . \quad (2)$$

Our measurements and our analysis depend only on the photopeak kinetic energy E ; we do not use the monochromator energy scale or the value of the binding energy. We label each spectrum by the photopeak mean energy E and electron energy within each spectrum we will call E_a .

To estimate the photoemission intensity, we decompose each photoemission spectrum into peak, tail, and background contributions. Figure 1 demonstrates the decomposition for $E = 264$ eV. Notice that the least-squares fit also provides the value of E . We employ simple functions for our fits. The Gaussian function for the photopeak, centered at E ,

$$G(E, E_a) = \frac{G(E)}{(2\pi)^{1/2}\sigma} e^{-(E_a - E)^2/4\sigma^2} \quad (3)$$

has an area $G(E)$ and a full width at half maximum (FWHM) equal to $2\sigma(2\ln 2)^{1/2}$. To mimic the increase in secondary emission caused by inelastic scattering of photoelectrons, the tail was chosen to be a Gaussian broadened step function:

$$T(E, E_a) = T(E) \left[\frac{1}{2} - \frac{1}{2} \operatorname{erf} \left(\frac{E_a - E}{2\sigma} \right) \right] \quad (4)$$

whose mean is at E and whose width is forced to be the same as the photopeak. The background is a scaled experimental electron emission spectrum M taken with $E = 30$ eV:

$$B(E, E_a) = B(E)M(E = 30, E_a). \quad (5)$$

From each least-squares fit we derive three numbers, the Gaussian area, $G(E)$ the photopeak position E , and—for reasons we now discuss—the background scale factor $B(E)$. The Gaussian peak width was allowed to vary to accommodate changes in monochromator resolution, but the width is not required for the analysis.

The Gaussian areas derived from our least-squares fits are proportional to the partial cross section we seek, but they also depend on the photon flux and electron analyzer transmission function. Calling the partial cross section $I(E)$, the photon flux $F(E)$, and the transmission function $A(E)$, we have the Gaussian areas

$$G(E) = F(E)A(E)I(E). \quad (6)$$

Note that the photon flux $F(E)$ is written as a function of photoelectron energy E . We mean for this function to represent all the instrumental intensity variations which influence the strength of the photoemission spectrum measured at kinetic energy E . Thus $F(E)$ contains the photon monochromator transmission, storage-ring current, slit widths, effective sample-photon-analyzer interaction region, and the spectrum integration time.

To remove the “photon flux” contribution we model the photoemission background as the product of photon flux, analyzer transmission, and an intrinsic background function $N(E, E_a)$:

$$M(E, E_a) = F(E)A(E_a)N(E, E_a). \quad (7)$$

We then assume that the intrinsic background does not depend on photon energy from 50–500 eV above the absorption edge. Thus a measurement of the electron emission spectrum for $E_a = 50$ –500 eV—when the photopeak is at $E = 30$ eV—is proportional to the intrinsic background:

$$M(E = 30 \text{ eV}, E_a) = F(30 \text{ eV})A(E_a)N(E_a). \quad (8)$$

When this spectrum is used as the photoemission background in the least-squares fits, a scale factor $B(E)$ is introduced [Eq. (5)]. Since we assume that the intrinsic background $N(E_a)$ does not depend on the position of the photopeak, the scale factor must be the ratio of the flux and transmission during the ARPEFS measurement to the flux and transmission during the background scan

$$B(E) = \frac{F(E)A(E_a)}{F(30 \text{ eV})A(E_a)} = F(E)/F(30 \text{ eV}). \quad (9)$$

Therefore the ratio of the photopeak area to the scale factor for the background function to the product of partial cross section and analyzer transmission

$$G(E)/B(E) = I(E)A(E)F(30). \quad (10)$$

Only the analyzer function remains. Based on the discussion in Sec. II, we take $A(E) = 1/E$, to give the partial cross section as

$$I(E) = cG(E)E/B(E) \quad (11)$$

with $c \sim E_p/F(30)$ an arbitrary, unknown constant.

Figure 2 demonstrates the $I(E)$ curves we obtained from applying these ideas to the S(1s) ARPEFS data. Notice that while description of our processing is complicated, the actual analysis is quite simple. The least-squares fits have three linear parameters (Gaussian area, tail area, and background scale) and two nonlinear parameters (Gaussian width and mean energy). Our least-squares fit computer program records these parameters on disk; when all the photoemission data have been analyzed, the parameters are read back in and the array algebra of Eq. (11) is performed.

Now we extract the oscillating part of the partial cross section according to

$$\chi(E) = (I - I_0)/I_0. \quad (12)$$

In principle, the atomic partial cross section I_0 could be approximated by the sulfur cross section calculated from some wave function for free atomic sulfur or a model for the S on Ni problem. From free-atom cross-section calculations¹⁵ we can see that the sulfur I_0 contains only very low-frequency information: We will make little error at the structurally important frequencies if we approximate

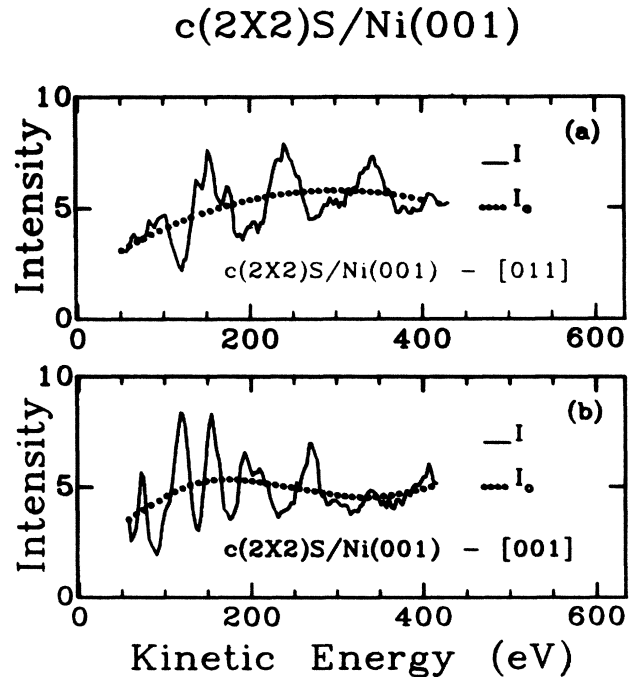


FIG. 2. Normalized angle-resolved-photoemission intensities as a function of photopeak energy and atomlike I_0 curves from least-squares fits for $c(2 \times 2)$ S/Ni(001). The solid curve is the photoemission intensities, and the dotted curve is the I_0 estimate. (a) Emission along [011], (b) emission along [001].

I_0 as the smooth part of I . Furthermore, as we discuss below, systematic errors in the measurement of I and the estimation of low frequencies in the Fourier transform invalidate any distinctions between the "correct" I_0 and our simple estimate.

Figure 2 shows our fit of $I_0(E)$ to a quadratic function of energy:

$$I_0(E) = aE^2 + bE + c \quad (13)$$

for the [011] experiment and a smooth spline for the [001] experiment. The resulting $\chi(E)$ from Eq. (12) is shown in Fig. 3.

This curve $\chi(E)$ is the ARPEFS. It represents the proportional change in partial cross section due to interference between direct and scattered photoemission. Our measured oscillations are very large, $\pm 50\%$ of the average value; the signal seems to be dominated by a few mid-range frequencies. In the next section we demonstrate that these oscillations can be analyzed to determine surface structures.

B. Possible sources of error

The procedure we selected to derive the extended fine structure from the photoemission measurements suffers from several systematic and random errors. In deriving the partial cross-section curve $I(E)$ from the photoemission measurements we must avoid five important limits to structural accuracy.

(i) *Cross-section variations.* As the photon energy is scanned, the inelastic electron spectrum $N(E_a)$ may change as the photoabsorption cross section for the levels which contribute to it change. Far from threshold these changes will be smooth decreases in secondary electron flux. Crossing a threshold will cause a sudden jump in flux. For S on Ni there are no absorption thresholds in the 500-eV photon energy range above the S(1s) edge, and, since we measured $N(E_a)$ at a photon energy near threshold where the cross section is large, we expect that our

background will be systematically too high at higher photon energies. This low-frequency error should be eliminated when $\chi(E)$ is formed. The EXAFS oscillations will also be superimposed upon the S(1s) photoabsorption cross section, but these oscillations are more than an order of magnitude smaller than the ARPEFS oscillations.¹

(ii) *Auger peak cross-section variation.* The inelastic electron spectrum measured with the photopeak at low kinetic energy should overestimate the size of the adsorbate Auger features. For example, the S LMM Auger region near 150 eV containing structure from cascade decay of the S(1s) hole was measured with a photon energy of 2504 eV, but was then used to fit photoemission spectra with photon energies near 2624 eV. The drop in the absorption cross section over this energy range will lead to a smaller least-squares fit coefficient $B(E)$ for the background in the Auger region than we would have obtained if we had measured the higher region with a photon energy closer to 2624 eV. Thus we will overestimate $I(E)$ near adsorbate Auger features. This problem is localized to energies near the Auger peaks and hence will have little influence on medium frequency oscillations.

(iii) *Storage-ring current loss.* The inelastic scattering curve was estimated by a single long-energy range scan of the background. The storage-ring current will drop by $\sim 5\%$ during this scan, leading to a slight underestimation of $M(E, E_a)$ at high E_a .

(iv) *Photon beam movement.* One further problem with the background fit method stems from the use of the double crystal JUMBO monochromator at the Stanford Synchrotron Radiation Laboratory (SSRL). Heat from the synchrotron beam on the first crystal expands it, changing the spectrometer equations of motion.¹³ While a static heat load can be compensated, synchrotron beam decay, beam loss, or reinjection changes the heat load. While the ~ 3 -eV energy shifts which accompany a doubling of beam current on injection do not affect our spectroscopy—we measure the kinetic energy—the beam movement on the sample can change the shape of the background, and the changing heat load will influence the monochromator resolution and thus the Gaussian photopeak width.

(v) *Photopeak line-shape function.* The choice of Gaussian photopeak plus Gaussian tail to represent the photoemission intensity is certainly oversimplified. Although the instrumental resolution is ~ 2.5 eV, our measured photopeak had a width of ~ 3.0 eV, indicating additional (e.g., lifetime) broadening. The tail contains electrons scattered inelastically in the sample and in the analyzer as well as the metallic response tail of Doniach and Sunjic.¹⁶ The processes would have to be investigated as functions of photoelectron kinetic energy to accurately characterize the photoemission line shape. Our much simpler function slightly underestimates the true line shape, giving a systematically low value for the photoemission intensity.

The conversion of photoelectron intensities to fine structure leads to two further systematic errors. First, the electron analyzer transmission is only approximately¹² proportional to $E_p/(\text{electron kinetic energy})$. Second, our method of determining I_0 empirically from our measurements will mix the true atomic partial cross section with

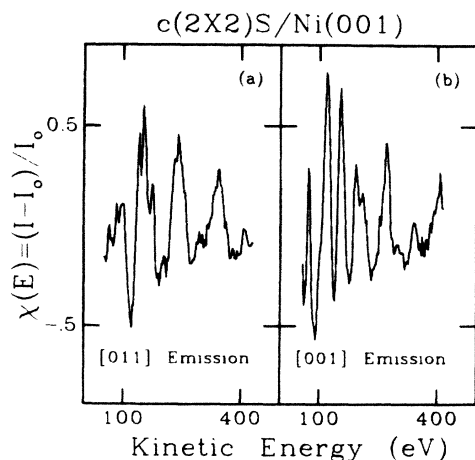


FIG. 3. ARPEFS oscillation $\chi(E)$ for $c(2 \times 2)\text{S}/\text{Ni}(001)$ versus electron kinetic energy according to Eq. (3). (a) [011] emission, (b) [001] emission.

very low frequency-interference oscillations and systematic errors of the types we have been discussing.

None of these systematic errors is expected to contribute to the midrange frequencies important for structure analysis. Except for the Auger intensity problem and the EXAFS modulation, these errors should lead to mild trends in the data which will be removed in the calculation of $\chi(k)$. The Auger problem will be concentrated at the kinetic energies of the Auger peak: The Fourier spectrum of this disturbance will be broad and will not peak at structure frequencies. As noted above the EXAFS is too small to be observed.

Our random errors come from the statistical accuracy of our photoemission measurement. Assuming no errors in the line shapes of the least-squares fits and assuming a normal distribution of noise, the standard error of the partial cross section σ_I divided by the partial cross section I , i.e., the inverse of the signal-to-noise ratio, will be given by

$$\left(\frac{\sigma_I}{I}\right)^2 = \left(\frac{\sigma_G}{G}\right)^2 + \left(\frac{\sigma_E}{E}\right)^2 + \left(\frac{\sigma_B}{B}\right)^2,$$

where σ_j , $j=G,E,B$ are the standard errors of each parameter in the formula for I . Each standard error will be proportional to the residual variance which—given our assumptions—will be proportional to the total number of counts in the spectrum. Numerical calculations of the standard errors show that the random errors will contribute an approximately flat background to the Fourier spectrum of our signal. For very low signal-to-noise power ratios, spurious peaks in this background could be misinterpreted or contribute erroneously to correct scattering peaks. Our spectrum has sufficient precision to avoid this problem.

IV. EXTRACTING GEOMETRY INFORMATION

In the preceding section the extended fine structure $\chi(E)$ was derived from a series of angle-resolved-photoemission measurements. In this section we analyze the fine structure to extract the geometry. We divide the entire procedure in two parts, Fourier analysis and multiple-scattering analysis. We will discuss errors after we have described the entire procedure.

A. Fourier transformation

There are three steps in the Fourier transform procedure: conversion from energy to momentum scales, tapering or autoregressive linear prediction, and Fourier transformation.

Conversion of the fine structure curve from a kinetic energy scale to a momentum scale uses the de Broglie relation,

$$E = \frac{\hbar^2 k^2}{2m},$$

to relate the electron energy to its wave-vector magnitude. For the electron energy we use the peak position E derived from the least-squares fit to eliminate any energy errors in the photon monochromator. As discussed in Ref.

17 the measured electron energy can be related to the energy of the electron during the scattering E_s by $E = E_s - E_0$, where E_0 is the solid's inner potential. Thus the wave number k for a kinetic energy E_k is given by

$$k = \frac{2m}{\hbar^2} (E + E_0)^{1/2}.$$

With this conversion we obtain $\chi(k)$ as a table of numbers $[k, \chi(k)]$ whose spacing in k depends on the energy spacing of the photoemission measurements and on E_0 . Unfortunately none of the subsequent analyses can process data with unequal increments in the abscissa. Therefore, we fit $\chi(k)$ locally to a numerical spline function and evaluate the spline on an equally spaced mesh of 128 points. Figure 4 shows the interpolated $\chi(k)$ for $E_0 = 10.5$ eV.

The second step in Fourier analysis is required to reconcile the concept of frequency analysis with the finite range of our experimental measurements. Our goal is the isolation of the path-length difference, $r_j - r_j \cos \theta_j$, from the experimental $\chi(k)$ which we believe is represented by a cosine series, Eq. (1), suggesting a Fourier-analysis procedure. As discussed in Ref. 18, direct Fourier series transformation of $\chi(k)$ would not be adequate: Fourier analysis assumes an infinitely long measurement range. Finite range data must be tapered smoothly to zero by a weighting function before Fourier analysis, or else some procedure such as the autoregressive linear prediction

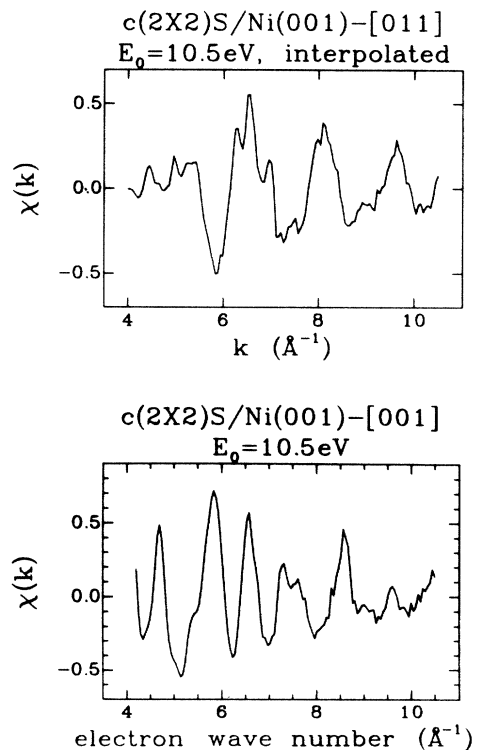


FIG. 4. ARPEFS oscillations after conversion to a momentum scale using an inner potential of 10.5 eV, and after interpolation to an even mesh of 128 points. (a) Emission along [011], (b) emission along [001].

(ARLP) described in Ref. 18 must be applied to estimate the frequencies of oscillation from a finite measurement range. The Fourier spectrum of the weighted data will be a smoothed version of the "real" spectrum of scattering amplitude versus path-length difference while the ARLP Fourier transform has higher resolution but is more sensitive to k dependence in the envelope which multiplies individual cosine oscillations. Therefore, we will present results from both procedures, using the ARLP spectra as a qualitative guide to the frequency spectrum. Since as will ultimately refine the geometry by direct comparison to the experimental oscillations, the choice between conventional and ARLP methods to solve the finite data range problem in the Fourier transform is not important.

Following the guidelines in Ref. 18 we multiply the interpolated $\chi(k)$ curve by a Gaussian centered at 7.5 \AA^{-1} and having a FWHM of 4 \AA^{-1} for the conventional taper weighting method. For the ARLP method, 64 autoregressive coefficients were fit to the data based on 14 singular values for the [001] experiment and 17 singular values for the [011] experiment; the ARLP was applied to extrapolate 128 points forward and backward, and the resulting oscillations were tapered with a Gaussian function centered at 7.5 \AA^{-1} and having a FWHM of 12.3 \AA^{-1} . This prepares the oscillations for Fourier transformation.

In the third and final step we apply the Fourier transform via the fast-Fourier-transform algorithm.¹⁹ Prior to transformation we add zeroes to give 2048 points; this increase interpolates the Fourier spectrum to give smooth peaks.¹⁸

The magnitude of the complex Fourier coefficients is displayed in Fig. 5 for the [011] experiment, and Fig. 6 for the [001] experiment. Since our unit for k is rad \AA^{-1} , the independent axis of our Fourier transform gives the path-length difference directly in angstroms. Each of the peaks in Figs. 5 and 6 represent one or more scattering in-

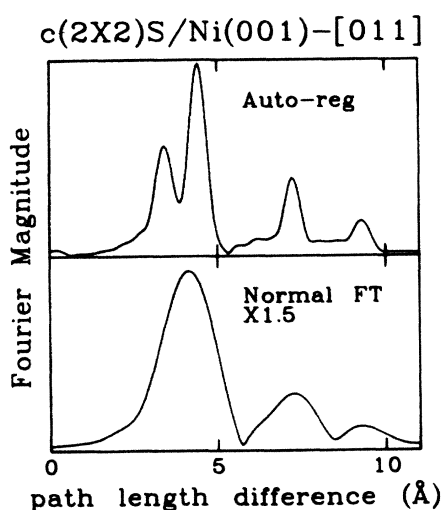


FIG. 5. Fourier-transform magnitudes versus scattering path length difference for k times the data in Fig. 3(a). In the lower panel, the conventional Fourier transform was applied, while the upper panel was obtained with the auto-regressive linear prediction method described in Ref. 18.

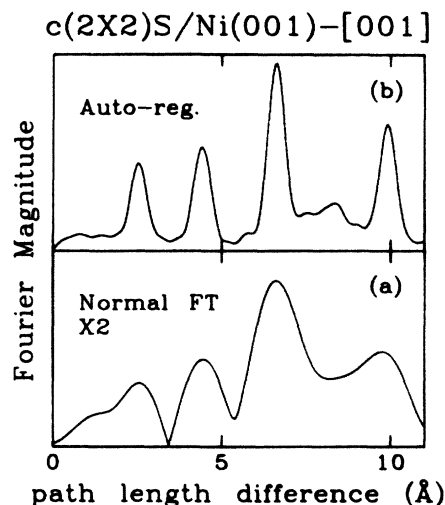


FIG. 6. Fourier-transform magnitudes versus scattering path length difference for k times the data in Fig. 3(b). In the lower panel, the conventional Fourier transform was applied, while the upper panel was obtained with the auto-regressive linear prediction method described in Ref. 18.

terferences. The peak position will be near the geometrical path-length difference, $r_j - r_j \cos \theta_j$, plus the linear part of the scattering phase shift ϕ_j . When comparing our results to plots of surface EXAFS Fourier transforms, recall that the EXAFS scale is usually chosen to display half of the geometrical path length since the only geometrical path-length difference in EXAFS is $2r_j$.

Our assignment of the peaks in the Fourier transforms to particular scattering path lengths is based on the empirical observation¹ that nearest neighbors and backscattering atoms dominate the spectrum. Recent theoretical studies of medium energy electron scattering provide a basis for this idea that nearest neighbors and backscattering atoms tend to dominate the ARPEFS. The essential physical arguments leading to the simplified picture for medium energy electrons are the following:

- (i) backscattering $\theta_j \sim 180^\circ$ dominates²⁰ over other angles $\theta_j \leq 30^\circ$,
- (ii) when the soft x-ray polarization vector is nearly parallel to the emission direction, side scattering is not excited,¹
- (iii) multiple scattering is primarily forward focusing,²¹ having no effect on the geometrical path-length difference,¹⁷
- (iv) curved wave-front corrections are required only for quantitative analysis of the ARPEFS curves,²²
- (v) correlated vibrational motion favors scattering from nearest neighbors,²³ and
- (vi) aperture integration favors backscattering.¹⁷

Thus Fourier-transform peaks arise primarily from a few identifiable atoms. Of course allowance must be made for possible interference due to near-lying path-length differences and the Ramsauer-Townsend splitting discussed in Ref. 24.

A cross-sectional view through the fourfold hollow adsorption site is shown in Fig. 7. Two peaks in the [011] spectrum (Fig. 5) are primarily due to three Ni nearest neighbors. The largest peak—at 4.4 Å—corresponds to scattering from the nearest-neighbor Ni directly behind the sulfur atom from the detector (atom 2 in Fig. 7). With a bond length of $r_j=2.2$ Å and a scattering angle $\theta_j=171^\circ$, the path-length difference is 4.37 Å. All of the amplitude factors favor this scattering atom. It lies along the peak in the angular distribution of the photoemitted p wave,¹⁷ it lies close to the emission center; and it backscatters into the detector.

The second largest peak—3.2 Å—corresponds to electron scattering from two nearest-neighbor Ni atoms (atom 1 in Fig. 7). These atoms are symmetrically located on either side of the plane containing the surface normal (the [001] direction) and the emission vector (the [011] direction). The scattering angle is 116° , giving a path-length difference of 3.12 Å. Despite the combined scattering power of two atoms, this peak is smaller than the 4.4-Å peak simply because both the photoemission final-state angular distribution and the scattering angular distribution are less favorable for 116° scattering.

The fourth nearest-neighbor atom should have a scattering angle of 83° and thus would appear at a path-length difference of 1.96 Å. However, we expect its amplitude to be small because the atom is near the node of the photoemitted wave: $\cos 83^\circ=0.12$. Therefore this atom does not produce a reliable peak in the Fourier transform. For example, it is small in Fig. 5, while it was somewhat larger in earlier analyses¹ using a slightly different transform weighting.

The peaks at 7.5 and 9.5 Å seem to correspond to backscattering atoms further away from S along the [011] axis. If we consider the 4.4-Å peak to be a member of a (011)

plane perpendicular to the emission direction, then the 7.5-Å peak would correspond to 4 atoms in the next (011) plane away from S (atoms 3 and 3' in Fig. 7) and the 9.5-Å peak would correspond to the atoms in the succeeding plane which lies directly behind the 4.4-Å Ni scatterer (e.g., atom 4 in Fig. 7).

Two peaks in the normal emission [001] experiment Fourier spectrum (Fig. 6) can be assigned in the same fashion as the [011] assignment. The 6.2-Å peak must be predominantly backscattering from the second-layer Ni atom directly below S since this atom is 180° from the detector in the [001] emission geometry. The peak near 10 Å should have a large contribution from atoms in the third Ni layer below S for the same reason. Atoms in the second Ni layer not directly in backscattering contribute the majority of the signal to the Fourier spectrum between 6.2 and 9 Å, but we cannot give more specific assignments without detailed calculation.

The most interesting features of the [001] Fourier transform are the two peaks below 5 Å which seems to defy a scattering path-length explanation. Both of these peaks can be attributed to scattering from the four nearest-neighbor Ni atoms in the first Ni layer below S even though the geometrical path-length difference for all four neighbors is near 3.5 Å where no Fourier peak is observed. The physical explanation for this Fourier peak splitting is a generalized Ramsauer-Townsend (GRT) resonance in the Ni scattering amplitude which simulates a beat envelope as k increases through 7.5 \AA^{-1} . We have discussed these peaks and their use in the measurement of the S—Ni bond length elsewhere; the results obtained by evaluation of the GRT resonance are in full agreement with the geometric parameters derived in this paper.²⁴

B. Multiple-scattering analysis

With the raw photoemission spectra reduced to ARPEFS oscillations and the Fourier spectra at hand, we can proceed to determine the structure. Previously, we have attempted to analyze the 4.4-Å backscattering peak in the [011] experiment by applying the Fourier back-transformation methods of EXAFS.¹ This analysis was based on the apparent success of single-scattering calculations to simulate the general features of the ARPEFS curve, but we now recognize¹⁷ that forward focusing is a fundamental feature of the photoelectron scattering. While the forward focusing does not change the oscillation frequency, it does change the oscillation amplitude and phase. Since the EXAFS-like analysis requires the phase to be known,³ we will not pursue that approach here.

Our alternative is a Fourier-filtering, least-squares fitting procedure which uses the Fourier spectrum to reduce the multiple parameter space of geometry variables without relying on the Fourier transform for the final structure analysis. The key element in this approach is the filtering of the ARPEFS to remove scattering path-length differences corresponding to all layers except the S overlayer and the first Ni layer. This filtered ARPEFS curve then depends upon a single geometrical parameter, the S—Ni bond length, or equivalently the S-Ni interlayer

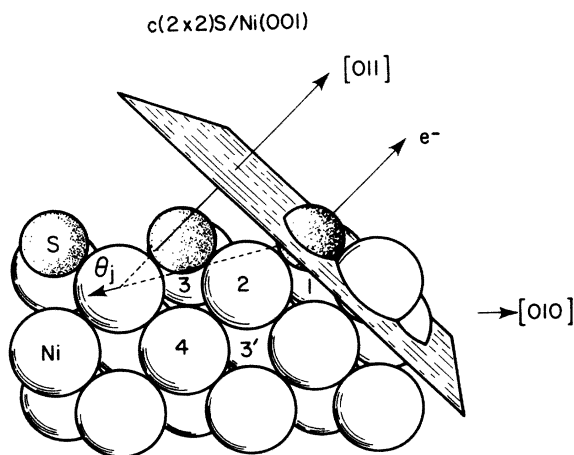


FIG. 7. Cross-sectional view of a fcc crystal (001) surface showing the experimental geometry for the [011] experiment. The angle-resolving detector is along the vector labeled e^- ([011] direction); the polarization vector is \hat{e} . The geometrical path-length difference is given by the bond distance from S to a scattering Ni atom plus the distance from the Ni atom to the plane perpendicular to the emission direction and passing through the S photoemitter.

spacing (d_1). Furthermore, the filtered curve contains only a restricted set of path-length differences and numerical simulation of the filtered curve even including multiple-scattering and curved-wave corrections is very economical. Once the S-Ni layer spacing is set, the spacing to the second layer can be optimized by selecting a new filter width which includes atoms scattering from the second layer.

For the [001] experiment, it is appropriate to filter the Fourier spectrum at 5 Å, isolating the two peaks split by the Ni-scattering resonance. As this analysis involves a discussion of the resonance, we have reported it separately²⁴ finding a S-Ni bond length of 2.20 ± 0.02 Å ($d_1 = 1.32 \pm 0.03$ Å).

For the [011] experiment, 5 Å was also chosen for the filter cutoff. This location is a minimum in the Fourier amplitude spectrum just above the 4.4-Å main back-scattering peak. To obtain the filtered ARPEFS spectrum we have simply zeroed the Fourier coefficients for frequencies above 5 Å and applied the fast Fourier inverse transform.

We recognize that the [011] experimental geometry is more difficult to align with our present apparatus than the normal emission [001] case, and we have noticed that our numerical simulations are very sensitive to the polar angle of emission. Thus we have performed a two-dimensional search in S-Ni interlayer spacing and emission polar angle to minimize the possibility that misalignment determines our result. Figure 8 gives the least-squares error surface for these variables. The numerical simulations were performed as described in Ref. 17 using the vibrational averaging, mean-free path, aperture damping, and scattering phase shift parameters given there. Moderate changes in the nonstructural parameters will change the size of the least-squares error but not the position of the minimum; conversely, we cannot reliably estimate the nonstructural parameters by least-squares fits of this kind. A clear minimum is evident in the surface at

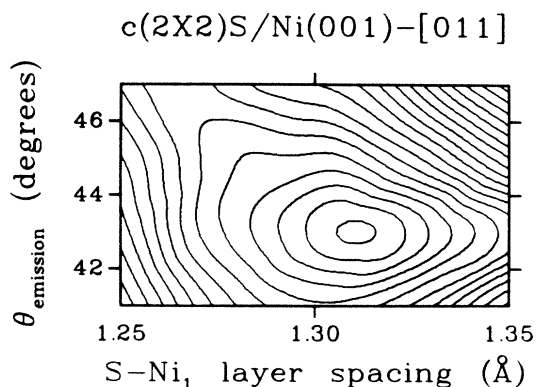


FIG. 8. Contour map of the least-squares error for fits of numerical simulations to data Fourier filtered at 5.1 Å from the [011] emission experiment. The horizontal axis gives the spacing along the crystal normal between the sulfur photoemitter and the first layer of Ni atoms (d_1). The vertical axis gives the variation of the polar angle of emission measured from the surface normal. Inner potential fixed at 10.5 eV.

43° emission angle and a S-Ni interlayer spacing (d_1) slightly above 1.30 Å, in good agreement with the results of the [001] experiment.

With the emission angle for the [011] experiment fixed at 43° and the S-Ni interlayer spacing fixed at 1.30 Å, we can return to the Fourier spectrum and filter for the second Ni layer. An appropriate filter location for the [011] experiment is 10.5 Å, but the [001] spectrum should be cut somewhat lower to avoid path lengths near 10 Å due to scattering from third-layer Ni atoms. However, we have used 10.5 Å for both experiments for convenience in the numerical simulation. The interlayer spacing between the second and third Ni layers is anyway equal to the bulk interlayer spacing (1.76 Å) to within our ability to measure it at this time.

In refining our geometry we must recognize that the $c(2 \times 2)$ symmetry observed in LEED does not constrain the Ni atoms in the second layer to be coplanar. Half the Ni atoms in this layer lie directly below S atoms (we call these atopped atoms) and half of these atoms lie below open spaces in the half monolayer coverage (we call these open atoms). The stability of the $c(2 \times 2)$ overlayer suggests that the local electronic environment of atopped and open Ni atoms could be different leading to the possibility that they would seek different equilibrium distances from the first Ni layer. Therefore, we have refined the positions of the atopped and open atoms separately, giving, for the [001] geometry, the two-dimensional least-squares error surface in Fig. 9. The dashed line running diagonally indicates the cut through this surface on which atopped and open atoms are coplanar. Along this line a clear minimum is found near 1.82 Å for the first and second

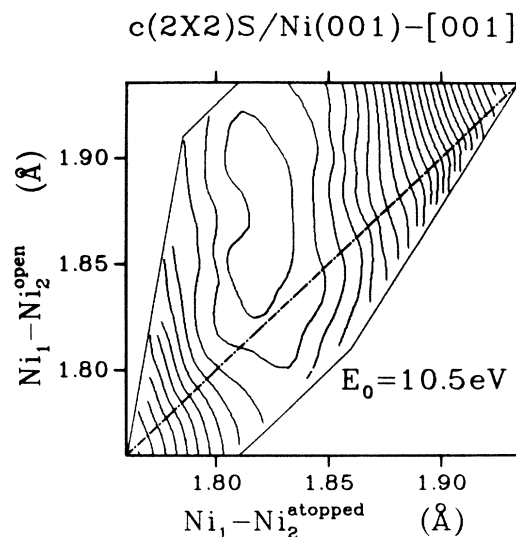


FIG. 9. Contour map of the least-squares error for fits of numerical simulations to Fourier filtered data (path lengths less than 10.5 Å) from the [001] emission experiment. The horizontal axis gives the spacing between the first layer of Ni atoms and those second-layer Ni atoms having S overlayer atoms on top of them (atopped atoms). The vertical axis gives the same quantity for second-layer Ni atoms having no S overhead (open atoms). The dotted-dashed line follows the constrained coplanar geometry. Inner potential fixed at 10.5 eV and d_1 at 1.30 eV.

Ni-layer spacing. To be more precise our measurement gives the distance between S and the second Ni layer of 3.12 Å which we combine with the spacing of the S and first Ni layers to give 1.82 Å for the Ni-Ni spacing. Relaxing the coplanar constraint, we see a broad minimum where the atopped Ni atoms stay near 1.82 Å below the first layer while the open Ni atoms move further down with a minimum near 1.87 Å.

The surface for the [011] experiment is similar (Fig. 10) along the coplanar constraint line having a minimum near 1.8 Å, but once the open atoms are allowed to vary independently, no minimum is found for spacings less than 1.94 Å. We discount the significance of this result because the [011] experimental geometry is not sensitive to the frequency change which accompanies the displacement of the open atoms—they move away at an oblique angle—but it is very sensitive to the amplitude of the scattering from these atoms. In fact, of all the scattering events which contribute to the two ARPEFS curves discussed here, calculations of scattering from open atoms in the [011] experiment, have the poorest agreement with experiment.

These comparisons of scattering calculations and Fourier-filtered experimental data rely on an accurate value for the inner potential used to construct the experimental momentum scale. We can estimate the maximum possible geometry error by calculating the least-squares error after optimizing the fit between experiment and theory with an adjustable inner potential. Since most of the ARPEFS signal is already contained in the 10.0-Å simulations, we recalculated the least-squares error surface for the [001] experiment comparing these simulations

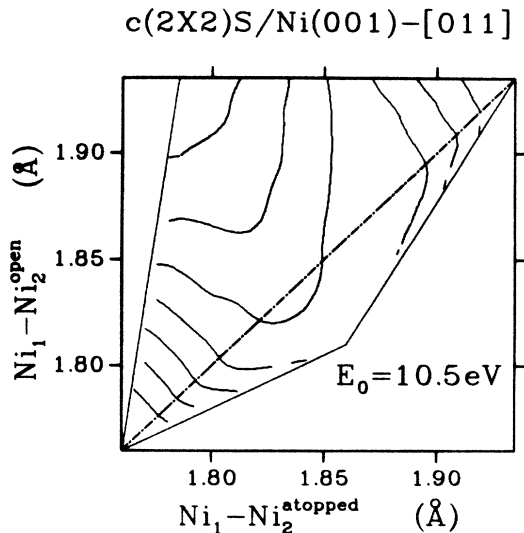


FIG. 10. Contour map of the least-squares error for fits of numerical simulations to Fourier-filtered data from the [011] emission experiment. The horizontal axis gives the spacing between the first layer of Ni atoms and those second-layer Ni atoms having S overlayer atoms on top of them (atopped atoms). The vertical axis gives the same quantity for second-layer Ni atoms having no S overhead (open atoms). The dotted-dashed line follows the constrained coplanar geometry. Inner potential fixed at 10.5 eV.

directly to the experimental oscillations on the experimental energy scale, allowing both the theoretical inner potential and overall scale factor to vary. The resulting surface is shown in Fig. 11. Since the minimum in the surface with fixed inner potential does not improve when the inner potential is varied, the minimum shifts, and, with the added flexibility of the scaling and shifting optimization, the minimum will be much broader. We find a broad minimum centered near 1.85 Å for atopped Ni atoms and 1.87 Å for open Ni atoms, a slightly greater expansion than that found with fixed inner potential.

The optimal inner potential varies monotonically with the spacing between the sulfur layer and the atopped Ni layer; when this spacing is, for example, 1.86 Å, the optimal inner potential is -7.8 eV and larger expansions give lower inner potentials. Thus as long as we believe that the inner potential should be near 10 eV, the error surface with variable inner potential represents our maximum error: Any restraint on the inner potential to bring it back toward 10 eV will bring the optimal geometry back toward 1.87 Å. We have also varied the inner potential in the analysis of the ARPEFS curves filtered at 5 Å by placing the filtered experimental data on an energy scale using the inverse of the original conversion of energy to momentum. Both the [001] and [011] experiments give unchanged optimal S-Ni spacing and optimal inner potentials between 10 and 11 eV. Thus we believe the variable inner potential surface result represents an upper bound to the interplanar spacing of 1.86 Å.

Finally, we have selected a fixed spacing of the sulfur and second Ni layers at 3.135 Å with atopped and open atoms coplanar and reoptimized the S-Ni interlayer spacing calculating all path lengths up to 10.5 Å and using the same two error criteria as discussed above. The error curves in Fig. 12 all have their minima slightly above 1.30 Å (d_1) (2.19 Å S-Ni bond length) with the [011] curve to the spacing being more sensitive.

We have based our quantitative analysis on the least-squares error criterion, but visual comparison of the curves confirms the conclusions of the numerical analysis. We can verify that $d_1 = 1.30 \text{ Å}$ fits the filtered ARPEFS better than $d_1 = 1.35 \text{ Å}$ as in Fig. 13; by comparing Figs. 14 and 15 we can certainly exclude a S to second-layer spacing of 3.06 Å in favor of one closer to 3.14 Å.

C. Possible sources of error

The paramount sources of error in our structure analysis are the value of the inner potential and the scattering phase shifts used in the multiple-scattering calculations. Substantially less important are the values chosen for the nonstructural parameters in the theory, which control the oscillation amplitude but not its phase or frequency.

We strongly emphasize that the precision of ARPEFS analysis relies on the energy width of the measurement. Over the course of a single oscillation, a constant phase error, due to inner potential or scattering phase shifts, will lead to significant apparent geometry changes. Only by comparing the oscillations over several cycles can this source of error be reduced. Furthermore, estimation of

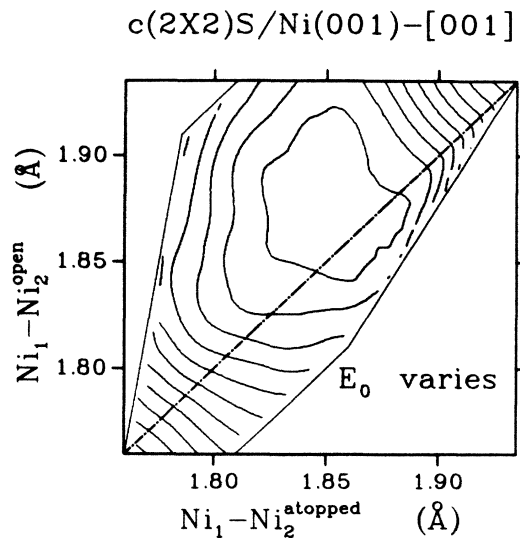


FIG. 11. Contour map of the least-squares error for fits of numerical simulations to data for the [001] emission experiment. The horizontal axis gives the spacing between the first layer of Ni atoms and those second-layer Ni atom having S overlayer atoms on top of them (atopped atoms). The vertical axis gives the same quantity for second-layer Ni atoms having no S overhead (open atoms). The dotted-dashed line follows the constrained coplanar geometry. The inner potential and overall scale of the theory was fitted to the data.

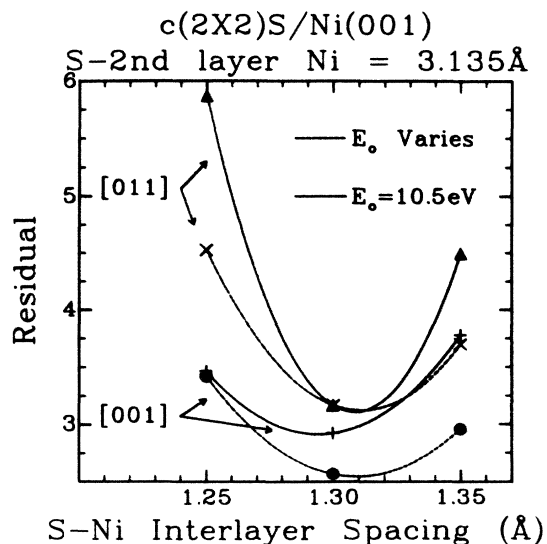


FIG. 12. Refinement of the S Ni-interlayer spacing with unfiltered data curves and a fixed S to second layer spacing of 3.135 Å. The upper curves are from the [011] experiment and the bottom pair are from the [001] experiment. The solid curves have a fixed inner potential for theory of 10.5 eV, while the dashed curves correspond to varying the scale and inner potential of the theory to best fit the data.

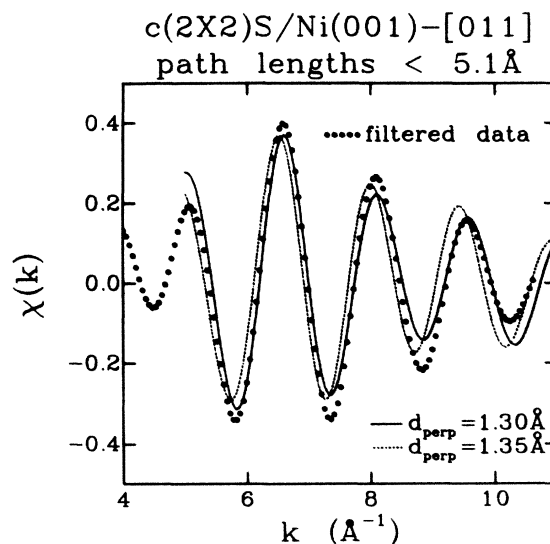


FIG. 13. Comparison of Fourier-filtered (5.1 Å) ARPEFS oscillations from the [011] experiment (solid circles), the numerical simulation for $d_1 = 1.30$ Å (solid line), and the numerical simulation for $d_1 = 1.35$ Å (dashed curve).

the atomiclike background I_0 severely distorts oscillations with a single cycle over the energy range, and the Fourier processing requires a maximum energy range for resolution of the Fourier peaks. Whenever several ARPEFS oscillations are covered in the measured range, the precision of the structure analysis should exceed 0.02 Å in interplanar spacings.

Quantitative bounds for the structural accuracy are more difficult to estimate. As we have discussed in the previous section, the inner potential is directly connected

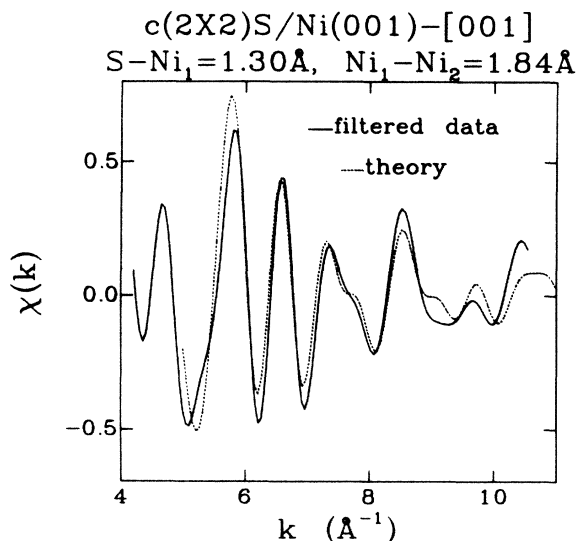


FIG. 14. Comparison of Fourier-filtered (10.5 Å) ARPEFS oscillations from the [011] experiment (solid curve) to the numerical simulation for $d_1 = 1.30$ Å and a S to first Ni-layer spacing of 1.84 Å (dashed curve). The atopped and open Ni atoms are coplanar in the theory curve.

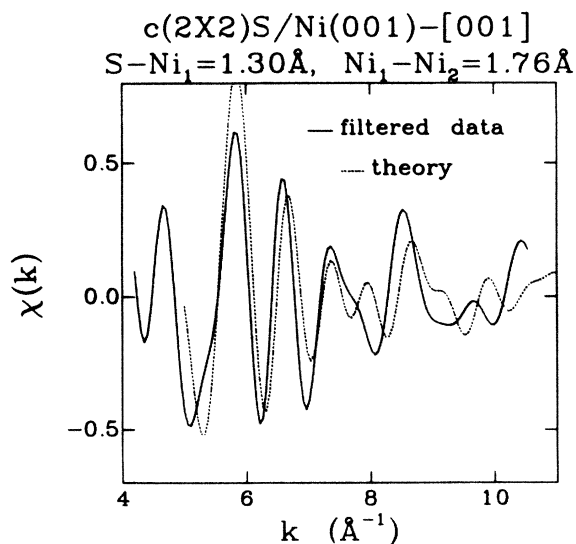


FIG. 15. Comparison of Fourier-filtered (10.5 Å) ARPEFS oscillations from the [011] experiment (solid curve) to the numerical simulation for $d_1=1.30$ Å and a S to first Ni-layer spacing of 1.76 Å (dashed curve) (the bulk interlayer spacing is 1.76 Å). The atopped and open Ni atoms are coplanar in the theory curve.

to the structure determination, and we find that a 2-eV error leads to a 0.02-Å error in geometry. The errors caused by the scattering phase shifts are more difficult to assess particularly since there does not seem to be published phase shifts in this energy range to which we may compare. As we are primarily sensitive to backscattering and forward scattering, we can conclude that the *frequency shift* caused by errors in the scattering phase shifts are likely to be negligible: We can see from published²⁵ EXAFS backscattering phase functions that change from Ni to Cu potentials would introduce a linear phase shift less than 0.02 Å, and since the linear part of the forward scattering phase function is less than 0.05 Å even a 50% error may be ignored. Exactly the opposite must be concluded about errors due to the *constant part* of these phase functions: The published backscattering phase functions have large changes in phase with atomic number, and the forward-scattering constant phase shift is large.

Moreover, there is a close connection between inner potential errors and errors in the constant part of the scattering phase function. This connection is exploited in the analysis of EXAFS data²⁶ by allowing the inner potential to vary. The procedure we followed in the previous section to vary the inner potential is analogous to the EXAFS analysis in that we might hope to cancel some errors in the constant phase with a variable inner potential, but we note several differences. First, the EXAFS inner potential is a complex weighted sum of absorption edge energies even when the scattering potential is exactly known: For all practical purposes the EXAFS inner potential is neither calculable nor measurable. The ARPEFS inner potential may be more accessible if only

because it is not connected to the photoabsorption process. Second, the EXAFS inner potential usually must also account for errors in phase shift functions caused by curved wave corrections, while our simulation curves include curved wave effects. And third, the EXAFS analysis usually concentrates on a single backscattering oscillation so that the floating inner potential need not work to correct amplitude errors while our floating inner potential may compromise between correcting phase errors and errors due to incorrect relative scattering amplitudes. Thus the simpler analysis of the 5-Å filtered data lead to consistent, physically reasonable inner potentials near 10.5 eV while the more complex comparison in Fig. 11 leads to more unusual values.

Until a thorough investigation of the scattering potentials in the intermediate energy range is complete, the errors caused by thermal averaging, aperture integration, and inelastic mean-free path may be ignored. It is obvious from the comparison of the numerical simulation in Fig. 12 that these values are not too far wrong: The overall magnitude of the oscillations is correct at high and low energy. Furthermore, the nonstructural parameters may be more properly investigated by studying them directly, i.e., through temperature and aperture variations.

V. DISCUSSION AND CONCLUSION

Although we are not yet in a position to quantify our accuracy, our results should be of comparable quality to other surface structure methods. The $c(2 \times 2)S/Ni(001)$ structure has been studied by LEED, normal photoelectron diffraction (NPD), and surface EXAFS. The $c(2 \times 2)S/Ni(001)$ system served as one of the prototype surface systems for LEED so that it is inappropriate to quote much of the earlier work. The most recent results^{4,27,28} agree on a S-Ni interlayer spacing d_1 of 1.3 ± 0.1 Å, corresponding to a S-Ni bond length of 2.19 ± 0.06 Å. The NPD experiment⁵ using the $S(2p)$ core level gave a S-Ni interlayer spacing of $d_1 = 1.30 \pm 0.04$ Å (S-Ni) bond length of 2.19 ± 0.03 Å). The surface EXAFS analysis⁶ gave a S-Ni bond length of 2.23 ± 0.02 Å equivalent to a $d_1 = 1.37 \pm 0.03$ Å. None of these measurements addressed the Ni-Ni interlayer spacing.

We conclude from our analysis of the two ARPEFS curves that $d_1 = 1.31 \pm 0.03$ Å (S-Ni bond 2.19 ± 0.02 Å). This is in excellent agreement with the LEED and NPD results, but—if we may trust the error bars—in only fair agreement with the EXAFS analysis. Given the uncertainty we have about the scattering potential, we cannot propose to select our result over the EXAFS one, but our agreement with the NPD results is gratifying because the measurements are similar to our [001] experiment while the theoretical analysis was based on multiple-scattering calculation using a quite different approach than we have applied here, including different scattering phase shifts.

We have no comparison for the Ni-Ni interlayer spacing of 1.83 ± 0.03 Å, or a 4% expansion compared to bulk Ni. This is equal to the expansion of the first two Ni layers on clean Ni reported by Demuth and Rhodin²⁹ but larger than the spacing, 1.78 ± 0.02 Å, reported by Demuth, Marcus, and Jepsen.³⁰ We also have some indi-

cation that Ni atoms in the second layer with S atoms overhead pulled out of the bulk somewhat.

Throughout our discussion we have been especially critical in our search for sources of inaccuracy and imprecision in our results. While we have explored a number of problems with our own measurement, we emphasize that ARPEFS measurements is carried in medium frequency oscillations of large amplitude: with modest care, baseline drift, and statistical noise will not limit the geometrical accuracy. However greater care is required in the experimental alignment: The ARPEFS oscillations are very sensitive to the surface structure and to the emission angle. This first ARPEFS measurement was made by adapting equipment and techniques not originally designed for surface structure determination. Once a vacuum-compatible apparatus is designed which can align

a surface with precision comparable to crystal alignment in x-ray crystallography, routine precision of 0.01 Å should be available for ARPEFS measurements. This chemically significant precision combined with the initial qualitative structure analysis available in Fourier transformation should make adsorbate structure determination by ARPEFS very attractive to the surface scientist.

ACKNOWLEDGMENTS

This work was supported by the Director, Office of Energy Research, Office of Basic Energy Sciences, Chemical Sciences Division of the U.S. Department of Energy under Contract No. DE-AC03-76SF00098. It was performed at the Stanford Synchrotron Radiation Laboratory, which is supported by the Department of Energy's Office of Basic Energy Sciences.

*Permanent address: Department of Physics, University of Petroleum and Minerals, Dhahran, 31261, Saudi Arabia.

†Permanent address: Physik-Department 20, Technische Universität München, D-8046 Garching bei München, West Germany.

¹J. J. Barton, C. C. Bahr, Z. Hussain, S. W. Robey, J. G. Tobin, L. E. Klebanoff, and D. A. Shirley, *Phys. Rev. Lett.* **51**, 272 (1983).

²P. A. Lee, *Phys. Rev. B* **13**, 5261 (1976).

³P. A. Lee and J. B. Pendry, *Phys. Rev. B* **11**, 2795 (1975).

⁴M. A. Van Hove and S. Y. Tong, *J. Vac. Sci. Technol.* **12**, 230 (1975).

⁵D. H. Rosenblatt, J. G. Tobin, M. G. Mason, R. F. Davis, S. D. Kevan, D. A. Shirley, C. H. Li, and S. Y. Tong, *Phys. Rev. B* **23**, 3828 (1981).

⁶S. Brennan, J. Stöhr, and R. Jaeger, *Phys. Rev. B* **24**, 4871 (1981).

⁷R. J. Madon and H. Shaw, *Catal. Rev. Sci. Eng.* **15**, 69 (1977).

⁸E. W. Plummer, B. Tonner, N. Holzwarth, and A. Liebsch, *Phys. Rev. B* **21**, 4306 (1980).

⁹P. J. Orders, R. E. Connelly, N. F. T. Hall, and C. S. Fadley, *Phys. Rev. B* **24**, 6163 (1981).

¹⁰Ni etch: 30% nitric acid, 10% sulfuric acid, 10% acetic acid, 30% glacial acetic acid, at 75°C. The faint white cloud which sometimes accompanies this etch is easily removed in the subsequent vacuum treatment.

¹¹S. D. Kevan, Ph.D. thesis, University of California, Berkeley, 1980.

¹²The analyzer has a $\pm 3^\circ$ circular entrance lens and a $2^\circ \times 4^\circ$ opening to the hemisphere after retardation or acceleration to the pass energy. For $E_p = 160$ eV, the transmission is independent of energy below 70 eV, falls like $[c(E)]^{-0.5}$ between 70 and 285 eV and falls like $[c(E)]^{-1}$ above 285 eV.

¹³Z. Hussain, E. Umbach, D. A. Shirley, J. Stöhr, and J. Feldhaus, *Nucl. Instrum. Methods* **195**, 115 (1982)

¹⁴J. R. Noonan and H. L. Davis in *Determinations of Surface Structures by LEED*, edited by P. M. Marcus and F. Jona (Plenum, New York, 1984), p. 449.

¹⁵S. Y. Tong (private communication).

¹⁶S. Doniach and M. Sunjic, *J. Phys. C* **3**, 285 (1970).

¹⁷J. J. Barton, S. W. Robey, and D. A. Shirley, "Theory of Angle-Resolved Photoemission Extended Fine Structure", Lawrence Berkeley Laboratory Report No. LBL-19324, and submitted to *Phys. Rev. B*.

¹⁸J. J. Barton and D. A. Shirley, Lawrence Berkeley Laboratory Report No. LBL-14758, 1985 (unpublished).

¹⁹E. O. Brigham, *The Fast Fourier Transform* (Prentice-Hall, Englewood Cliffs, N.J., 1974).

²⁰P. J. Orders and C. S. Fadley, *Phys. Rev. B* **27**, 781 (1983).

²¹S. Y. Tong and C. H. Li, in *Chemistry and Physics of Solid Surfaces*, edited by R. Vanselow (Chemical Rubber Co., Cleveland, 1982), Vol. III, p. 287.

²²J. J. Barton and D. A. Shirley, *Phys. Rev. B* **32**, 1892 (1985).

²³M. Sagurton, E. L. Bullock, and C. S. Fadley, *Phys. Rev. B* **30**, 7332 (1984); P. J. Orders, B. Sinković, C. S. Fadley, R. Trehan, Z. Hussain, J. Lecante, *Phys. Rev. B* **30**, 1838 (1984).

²⁴J. J. Barton and D. A. Shirley, Lawrence Berkeley Laboratory Report No. LBL-19325, 1986, and *Phys. Rev. B* (to be published).

²⁵B. K. Teo and P. A. Lee, *J. Am. Chem. Soc.* **101**, 2815 (1979).

²⁶P. A. Lee, P. H. Citrin, P. Eisenberger, and B. M. Kincaid, *Rev. Mod. Phys.* **53**, 769 (1981).

²⁷Y. Gauthier, D. Aberdam, R. Baudoing, *Surf. Sci.* **78**, 339 (1978).

²⁸J. E. Demuth, D. W. Jepsen, and P. M. Marcus, *Phys. Rev. Lett.* **31**, 540 (1973).

²⁹J. E. Demuth and T. N. Rhodin, *Surf. Sci.* **42**, 261 (1974).

³⁰J. E. Demuth, P. M. Marcus, and D. W. Jepsen, *Phys. Rev. B* **11**, 1460 (1975).